Destruction of trapping oscillations

G. Dimonte[a] and J. H. Malmberg

Department of Physics, University of California at San Diego, La Jolla, California 92093

(Received 30 June 1977; final manuscript received 20 January 1978)

A somewhat unconventional traveling wave tube was built to investigate the nonlinear behavior of the beam-plasma instability beyond the first trapping oscillation of the wave amplitude. In the small cold beam limit, the equations governing the evolution of the beam-plasma instability are mathematically identical to those describing the traveling wave tube. The traveling wave tube has the advantage that the slow wave structure will remain linear for the wave amplitudes reached in the experiments; furthermore, it does not introduce noise. Five trapped particle oscillations are observed following the saturation of a single launched wave. Two mechanisms for destroying these oscillations have been found. The first involves wave damping and can occur for decrements smaller than 0.01 k_0. The second is a result of the modulation of the main wave by unstable sidebands. In addition to the experiments, the equations which describe the interaction are solved numerically. The experimental observations are in excellent agreement with the results of the numerical calculations.

I. INTRODUCTION

The single wave trapping model[1-4] has been very successful in describing the initial stage of the nonlinear interaction between a small cold beam and a plasma. The essential feature of the model is that after many *e* foldings, the bandwidth of this instability is so narrow that the beam electrons interact with a wave which is nearly monochromatic, namely, the fastest growing wave. This wave grows until it traps the beam electrons, thereby saturating the instability. As the trapped particles slosh back and forth in the wave potential, the amplitude oscillates as a result of energy conservation in the laboratory frame.

The predictions of the single wave model agree completely with the experimental observations[5-10] through the initial trapping and up to the first amplitude oscillation. Beyond this point, the plasma experiments universally exhibit a rapid decay of the saturated wave rather than the persistent trapped particle oscillations predicted by the theory.[2-4] During the first amplitude oscillation the wave spectrum is broadened and (as was expected[1]) the single wave model is no longer applicable. Therefore, the initial nonlinear development of this instability is well understood, but the subsequent development remains to be explained.

The decay of the main wave is not well understood experimentally because there are many processes which may be responsible. They fall into the following three classes: (1) mechanisms involving the nonlinear motion of the beam electrons and the linear response of the plasma, (2) nonlinearities in the background plasma, and (3) characteristics of laboratory plasmas. An example of the first class is the sideband instability[11-13] in which waves at neighboring frequencies grow to large amplitude and detrap the particles. The second class is comprised of the nonlinearities[14-17] in the background plasma which occur for large beam strengths, typically $n_b/n_p \geq 1\%$. Simulations by Kainer *et al.*[14] show that plasma electrons can be trapped by the saturated wave when the trapping width is large. In this case, the background plasma is not a linear dielectric and the wave amplitude oscillations do not occur. Others[15-17] have demonstrated that if the amplitude of the main wave exceeds certain thresholds, the plasma is susceptible to a variety of parametric instabilities which may compete with trapping as a saturation mechanism. Since many beam-plasma systems employ strong beams, these nonlinear processes may contribute to the nonlinear decay of the main wave in these experiments. Third, laboratory plasmas suffer from density gradients, which may affect the evolution of the instability, and low frequency potential fluctuations, which can confuse the measurements.

In order to avoid problems associated with the background plasma, we built a somewhat unconventional traveling wave tube[18] to investigate the late-time development of the beam-plasma instability. The replacement of the plasma with a slow wave structure allows us to isolate effects which are due solely to the beam dynamics from those which result from the background plasma. In the small cold beam limit, the plasma acts essentially as a linear dielectric medium capable of supporting slow space charge waves. Therefore, this replacement does not alter the basic features of the wave-particle interaction. This is demonstrated by the fact that the equations of the single wave model[2-4] are identical to Nordsieck's[19] working equations for the nonlinear interaction in a traveling wave tube. The traveling wave tube, however, has advantages over beam-plasma systems in that the slow wave structure (i) will remain linear for all amplitudes reached in our experiments and (ii) does not introduce noise.

Of course, traveling wave tubes have been investigated extensively.[18-23] The equations for the nonlinear interaction were first solved by Nordsieck.[19] The saturation mechanism was established experimentally as beam trapping by Cutler[21] with measurements of the phase space distribution. However, the investigation of the nonlinear interaction has been limited to the initial saturation region because the primary application for traveling wave tubes is as a broadband and/or high pow-

---

[a] Present address: TRW Systems, Redondo Beach, Calif 90278.

0031-9171/78/2107-1188$00.90

er amplifier. Consequently, the investigators had no compelling reasons to study the interaction much beyond saturation.

In addition to the experiments, we have numerically solved the working equations of Tien's[23] model, which is essentially the single wave model with detuning, damping, and finite beam strength corrections included. This allows us to compare theory directly with our experimental results. Also, the diagnostic capability inherent in the computer simulation is helpful in clarifying the behavior of this instability.

Our basic findings are as follows: Experimentally, we observe over five trapped particle oscillations in the wave amplitude following the growth and saturation of a single launched wave. The accompanying nonlinear wave phase is also measured. It oscillates at half the bounce length in agreement with theory. In addition, we find that the wave phase oscillations influence the bounce length in a significant way. We have found two ways of destroying the trapping oscillations. The first mechanism involves the main wave only. As a result of dissipation in the slow wave structure, the trapping oscillations of the wave amplitude can have very deep minima. These trigger large and rapid phase shifts which disrupt the delicate phase relation between the trapped particles and the wave potential in such a manner as to abruptly detrap the particles. The second mechanism is a result of unstable sidebands growing to large amplitude. These modulate the main wave to produce beat minima which allow the particles to become detrapped. The detrapping, induced by either method, leads to particle mixing in phase space which precludes further trapping oscillations.

Our measurements agree with our numerical solutions. Both detrapping processes are well described by theory.

The remainder of the paper is organized as follows: in Sec. II the theory is reviewed. Section III contains a description of the experimental apparatus and the measurement techniques. In Sec. IV we present the results of the single wave experiments. In Sec. V we describe the destruction of the trapping oscillations as a result of wave dissipation. In Sec. VI we investigate the influence of the wave phase shifts on the bounce length. In Sec. VII we describe the effects of unstable sidebands on the main wave. Our conclusions form Sec. VIII.

II. THEORY

In this section we review the theory of the wave-particle interaction in a traveling wave tube and compare it with the corresponding plasma theory. The linear theory is that of Pierce.[18] For the nonlinear description we adopt Tien's model,[23] which extends Nordsieck's[19] analysis to include finite beam strength. However, the space charge force will be neglected in the nonlinear calculations for reasons discussed in part B. We solve the model equations numerically in order to compare the theoretical predictions directly with our experimental results.

A. Linear theory

In linear theory Pierce[18] treats the slow wave structure (circuit) as an equivalent transmission line which supports an electromagnetic wave capable of interacting resonantly with an electron beam through an interaction impedance

$$R = \langle E_z^2\rangle_b / 2k_{0r}^2 P \ , \tag{1}$$

where $\langle E_z^2\rangle_b$ is the square of the axial electric field averaged over the beam cross section, k_{0r} is the real part of the wavenumber, and P is the average power in the wave, all in the absence of the beam. The spatial evolution of the wave potential is described by a wave equation which has a source term due to the beam charge density. The motion of the beam particles is described by the equations of motion and continuity. They will be discussed further in part B. If we consider perturbations of the form $\exp[i(\omega t - kz)]$ and look for spatially varying solutions, the determinental equation, Eq. (7.9) of Ref. 18, becomes

$$(k - \omega/u_0)^2 = \frac{2k_0 k^2 C^3 \omega/u_0}{k_0^2 - k^2} + 4QC\, C^2 k^2 \ , \tag{2}$$

where ω is the wave frequency, and u_0 is the unperturbed beam velocity. $k_0 = k_{0r} + ik_{0i}$ is the complex wavenumber in the absence of the beam, where k_{0i} is the damping decrement, C is Pierce's gain parameter, and QC is the space charge parameter.

The gain parameter C is defined by Pierce as

$$C = (I_0 R/4V_0)^{1/3} \ , \tag{3}$$

where I_0 is the dc beam current and V_0 is the beam voltage. If the slow wave structure is the plasma of a beam-plasma system of infinite extent, C becomes $\{(\omega_{pb}/k_{0r}u_0)^2[u_0/\omega(\partial\epsilon/\partial k)_{\omega, k_0}]\}^{1/3}$ which corresponds to the basic scaling parameter of the small cold beam theory,[4] i.e., $(\eta'/2)^{1/3}$. ω_{pb} is the plasma frequency of the beam and $\epsilon = \epsilon(\omega, k)$ is the dielectric constant of the plasma.

The space charge parameter QC in Eq. (2) is calculated[24] to be

$$QC = \frac{1}{4C^2}\left(\frac{\omega_{pb} R_q/\omega}{1 + \omega_{pb} R_q/\omega}\right)^2 \simeq \left(\frac{\omega_{pb} R_q}{2C\omega}\right)^2 \ . \tag{4}$$

The finite size plasma frequency reduction factor R_q is calculated by Branch and Mihran[25] for various geometries. The QC parameter is basically a measure of the electrostatic force between beam electrons which results from the linear density perturbation produced by the circuit wave; as such it separates the fast and slow branches of the beam dispersion relation. In beam-plasma systems, this force is significant unless $(n_b/n_p)^{1/3} \ll 1$. By solving Eq. (2) numerically, Birdsall and Brewer[24] showed that the fastest growing wave occurs for a detuning near $k_{0r}u_0 - \omega \simeq \omega_{pb}R_q \simeq \omega C(4QC)^{1/2}$, that is, near the intersection of the circuit dispersion relation and the unperturbed slow beam branch.

We define the detuning parameter

$$b \equiv (k_{0r}u_0 - \omega)/\omega C \ , \tag{5}$$

the damping coefficient

$$d \equiv -k_{0i} u_0 / C\omega \quad , \tag{6}$$

and expand k about ω/u_0 to obtain

$$k = (1 + iC\delta)\,\omega/u_0 \quad , \tag{7}$$

where δ is complex and $O(1)$. Then, Eq. (2) can be rearranged to the form found in Ref. 24

$$\left(\delta + \frac{i(4QC)^{1/2}}{1 - C(4QC)^{1/2}}\right)\left(\delta - \frac{i(4QC)^{1/2}}{1 + C(4QC)^{1/2}}\right)$$
$$\times(\delta + ib + d)[C(\delta - ib - d) - 2i]$$
$$= 2(\delta C - i)^2\left(\frac{1 + Cb - iCd}{1 - 4QC\,C^2}\right) \quad . \tag{8}$$

In the limit $C \to 0$ and $QC \to 0$, Eq. (8) takes the familiar form[26] $\delta^2(\delta + ib + d) = -i$.

We solve Eq. (8) numerically for the scaled growth rate δ as a function of C, b, d, and QC. Since these parameters also characterize the nonlinear interaction, it is essential to determine them using linear measurements such as the growth rate. This is done in Sec. III.

B. Nonlinear theory: Single wave

The equations describing the nonlinear interaction in a traveling wave tube consist of (i) the transmission line wave equation for the electric field, (ii) the equation of motion for the beam electrons, and (iii) the charge continuity equation. For the electrostatic modes of a beam-plasma system, the wave equation is replaced with Poisson's equation.[2-4] When C, i.e., $(\eta'/2)^{1/3}$ is small, the plasma may be treated linearly and the two calculations lead to an identical set of equations. Nordsieck solved these equations for $C \ll 1$. The analysis has been extended[22,23] to higher order in C and to include space charge forces. Hess[27] compares the slightly different approaches and finds that they yield similar results. We adopt Tien's model (with wave damping included) because the equations are easier to solve numerically.

We neglect the space charge force, which is the repulsive force between beam electrons. For finite C, the model used to evaluate this force is questionable beyond the point where the electrons overtake one another because the calculated space charge potential energy decreases as the particles are bunched.[27] For $QC < 0.28$ and $b < 1.5$, Hess finds that the space charge force does not qualitatively alter the solution. Consequently, the inclusion of this force is of dubious benefit and it increases the computational cost considerably (one hundredfold for 600 particles). Of course, this simplification limits the applicability of our calculations, but only in a minor way for the parameter range in which we operate, i.e., $QC < 0.30$. When weak beams are employed, the predictions of the calculations (e.g., saturation power, bounce length, etc.) agree with measurements to within a few percent. For strong beams, the discrepancy increases to 20%. We attribute this error in the calculations for strong beam cases to our neglect of the space charge force.

If the slow wave structure is viewed as a transmission line and the beam is treated as a distributed generator, the circuit equation takes the form[22]

$$\frac{\partial^2 V}{\partial t^2} - \frac{\omega^2}{k_{0r}^2}\frac{\partial^2 V}{\partial z^2} + 2\omega C d\,\frac{\partial V}{\partial t} = \frac{\omega R}{k_{0r}}\frac{\partial^2 \rho}{\partial t^2} + 2\,\frac{\omega^2}{k_{0r}}\,CdR\,\frac{\partial \rho}{\partial t} \quad , \tag{9}$$

where $V = V(z,t)$ is the wave potential and $\rho = \rho(z,t)$ is the beam charge density (charge per unit length). In the small cold beam theory,[2-4] Eq. (9) would be replaced by Poisson's equation. The equation of motion is

$$m\,\frac{d^2 z}{dt^2} = e\,\frac{\partial V}{\partial z} \quad . \tag{10}$$

The orbit solutions of Eq. (10) determine the behavior of ρ through a Lagrangian formulation of the problem. As such, the solution will be a function of the initial position of an electron z_0, i.e., $z = z(z_0, t)$. Then, charge conservation requires that the charge $\rho(z_0, 0)dz_0$ due to electrons whose initial positions lie in the range z_0 to $z_0 + dz_0$ equal the charge $\rho(z,t)\,dz$ at some position z, that is,

$$\rho(z,t)dz = \rho(z_0, 0)dz_0 \quad . \tag{11}$$

If z_0 is taken to be near the entrance to the tube where the beam is unmodulated, the initial charge density is $\rho(z_0, 0) = I_0/u_0$.

We now introduce the independent variables. The scaled distance along the tube is

$$y \equiv C\,\omega z/u_0 \quad . \tag{12}$$

The entrance phase for an electron is

$$\phi_0 \equiv \omega t_0 = \omega z_0/u_0 \quad , \tag{13}$$

where t_0 is the time at which an electron enters the tube at $z = 0$. This can be thought of as a "tag" for electrons. When, for computational purposes, the beam is divided into N charge sheets per period, the initial phases are $\phi_{0j} = 2\pi j/N$, $j = 1, 2, \ldots, N$.

We define the dependent variables; the phase displacement

$$\phi(y, \phi_0) \equiv \omega(z/u_0 - t) \quad , \tag{14}$$

the instantaneous velocity

$$dz/dt \equiv u_0[1 + Cq(y, \phi_0)] \quad , \tag{15}$$

and the wave potential

$$V(z,t) \equiv V_1(z,t) + V_2(z,t) \quad , \tag{16}$$

where

$$V_1 = 4C^2 V_0 A(y)\cos[\phi - \theta(y)] \quad ,$$
$$V_2 = \frac{2C^3 V_0}{(1 + Cb)} \times \left\{ A(y)\left(\frac{d\theta(y)}{dy} + b\right)\cos[\phi - \theta(y)] - \frac{dA(y)}{dy}\,\sin[\phi - \theta(y)] \right\} ,$$

where $A(y)$ and $\theta(y)$ are the slowly varying amplitude and phase of the wave, respectively. V_2 is a finite C correction to the first-order term in the wave potential V_1. Since $C \ll 1$, we notice that $V_2 \ll V_1$.

In terms of the normalized variables Eqs. (9)–(11) become

$$\frac{dA(y)}{dy} = -\int_0^{2\pi} \frac{d\phi_0}{2\pi} \frac{\sin[\phi(y,\phi_0) - \theta(y)]}{1 + C\,q(y,\phi_0)} - dA(y) \ , \tag{17}$$

$$\frac{d\theta(y)}{dy} + b = \frac{1}{A(y)} \int_0^{2\pi} \frac{d\phi_0}{2\pi} \frac{\cos[\phi(y,\phi_0) - \theta(y)]}{1 + Cq(y,\phi_0)} \ , \tag{18}$$

$$\frac{d\,\phi(y,\phi_0)}{dy} = \frac{q(y,\phi_0)}{1 + Cq(y,\phi_0)} \ , \tag{19}$$

$$\begin{aligned}[1 + Cq(y,\phi_0)] \frac{dq(y,\phi_0)}{dy} &= 2A(y) \sin[\phi(y,\phi_0) - \theta(y)] \\ &\quad - C\left\{\frac{dA(y)}{dy} \cos[\phi(y,\phi_0) - \theta(y)]\right. \\ &\quad \left. + A(y)\left(\frac{d\theta(y)}{dy} - b\right) \sin[\phi(y,\phi_0) - \theta(y)]\right\} \ .\end{aligned} \tag{20}$$

Terms $O(C^2)$ and $O(Cd)$ have been neglected. In the limit where $C \to 0$, Eqs. (17)–(20) reduce to Eqs. (17) and (20) of Ref. 4. The additional terms in (17)–(20) enter because the perturbations in the particle velocity and the wave amplitude and phase are finite; that is, they are finite C corrections for spatially evolving systems. Analogous terms would appear in the small cold beam theory if the calculation is carried out to one higher order in $(\eta'/2)^{1/3}$.

In terms of the normalized variables, the wave power averaged over a period becomes[23] to $O(C^2)$

$$\langle P \rangle_{T_0} = 2C A^2(y) I_0 V_0 \ . \tag{21}$$

Equations (17)–(20) lead to two interesting conservation equations. If we divide Eq. (20) by $1 + Cq$, integrate over all initial particle phases and combine with Eqs. (17) and (18), we find momentum balance

$$\frac{d}{dy}\left[\frac{1}{(1+Cb)} \int_0^{2\pi} \frac{d\phi_0}{2\pi} q(y,\phi_0) + A^2(y)\right] = -2dA^2(y) \tag{22}$$

in the initial beam frame. This momentum balance requires that the wave amplitude oscillate as the particles rotate coherently in phase space. Notice that the wave phase shifts do not enter. In the limit $C \to 1$ we can multiply Eq. (20) by $q = d\phi/dy$, integrate over all initial particle phases and combine with Eqs. (17) and (18) to obtain a simplified expression for energy balance in the initial beam frame

$$\begin{aligned}\frac{d}{dy}\left[\int_0^{2\pi} \frac{d\phi_0}{2\pi} \frac{q^2(y,\phi_0)}{2} + \left(\frac{2d\theta(y)}{dy} + b\right) A^2(y)\right] \\ = -2d\,\frac{d\theta(y)}{dy} A^2(y) \ .\end{aligned} \tag{23}$$

Since the wave amplitude varies in order to satisfy momentum balance, wave phase shifts $d\theta/dy$ are necessary to simultaneously balance energy flow according to Eq. (23). In the absence of damping Eqs. (22) and (23) correspond to conservation of momentum and energy,[4] respectively, in the initial beam frame.

C. Nonlinear theory: Many waves

The nonlinear model can be expanded to include many waves.[13,28] Experimentally, we find that two additional waves are sufficient to destroy the trapping oscillations of the main wave; therefore, we shall consider a system with only three waves. In general, the interaction impedance R is a function of ω and k. However, in order to reduce the number of characteristic parameters to a manageable level, we assume R is identical for all three waves and that the wave-particle interaction is weak, $C \ll 1$.

We consider three waves of frequency $\omega_j = \omega_0 + j\Delta\omega$, $j = 0, \pm 1$ where ω_0 is an integer multiple of $\Delta\omega$, $\omega_0 = m\Delta\omega$. The latter requirement is necessary to satisfy the periodic boundary conditions imposed in the calculation. Each wave has a wavenumber k_{0j} which satisfies the circuit dispersion relation in the absence of the beam. The potential for the jth wave is assumed to have the form

$$V_j(z,t) = 4V_0 C^2 A_j^2 \cos(\alpha_j \phi - \theta_j) \ , \tag{24}$$

where

$$\phi(z,t) \equiv \omega_0(z/u_0 - t) \ , \tag{25}$$

$$\alpha_j \equiv \omega_j/\omega_0 = 1 + j/m \ , \tag{26}$$

where $A_j(z)$ and $\theta_j(z)$ are the slowly varying amplitude and phase of the jth wave. Each mode satisfies the wave equation independently. The equation of motion becomes

$$m\frac{d^2 z}{dt^2} = e \sum_{j=0,\pm 1} \frac{\partial V_j}{\partial z} \ . \tag{27}$$

The instantaneous particle velocity remains defined by Eq. (15). Charge conservation is given by Eq. (11).

We define the two independent variables,

$$y \equiv \omega_0 C z/u_0 \ ; \quad \phi_0 \equiv \omega_0 T_0 \ , \tag{28}$$

the detuning parameter

$$b_j \equiv (k_{0rj} u_0 - \omega_j)/C\,\omega_j \ , \tag{29}$$

and the damping coefficient

$$d_j \equiv -k_{0ij} u_0/C\,\omega_j \ . \tag{30}$$

In terms of the dimensionless variables, the wave equations and the equations of motion and continuity reduce to

$$\begin{aligned}\frac{dA_j(y)}{dy} \\ = -\alpha_j \int_0^{2\pi m} \frac{d\phi_0}{2\pi m} \sin[\alpha_j \phi(y,\phi_0) - \theta_j(y)] - \alpha_j d_j A_j(y) \ ,\end{aligned} \tag{31}$$

$$\begin{aligned}\frac{d\theta_j(y)}{dy} + \alpha_j b_j = \frac{\alpha_j}{A_j(y)} \\ \times \int_0^{2\pi m} \frac{d\phi_0}{2\pi m} \cos[\alpha_j \phi(y,\phi_0) - \theta_j(y)] \ , \quad j = 0, \pm 1 \ ,\end{aligned} \tag{32}$$

$$\frac{d\phi(y,\phi_0)}{dy} = q(y,\phi_0) \ , \tag{33}$$

$$\frac{dq(y,\phi_0)}{dy} = 2 \sum_{j=0,\pm 1} \alpha_j A_j(y) \sin[\alpha_j \phi(y,\phi_0) - \theta_j(y)] \ . \tag{34}$$

These scaled equations are similar to those in Matsiborko *et al.*[13] and are given in more generality by Scherba and Rowe.[28]

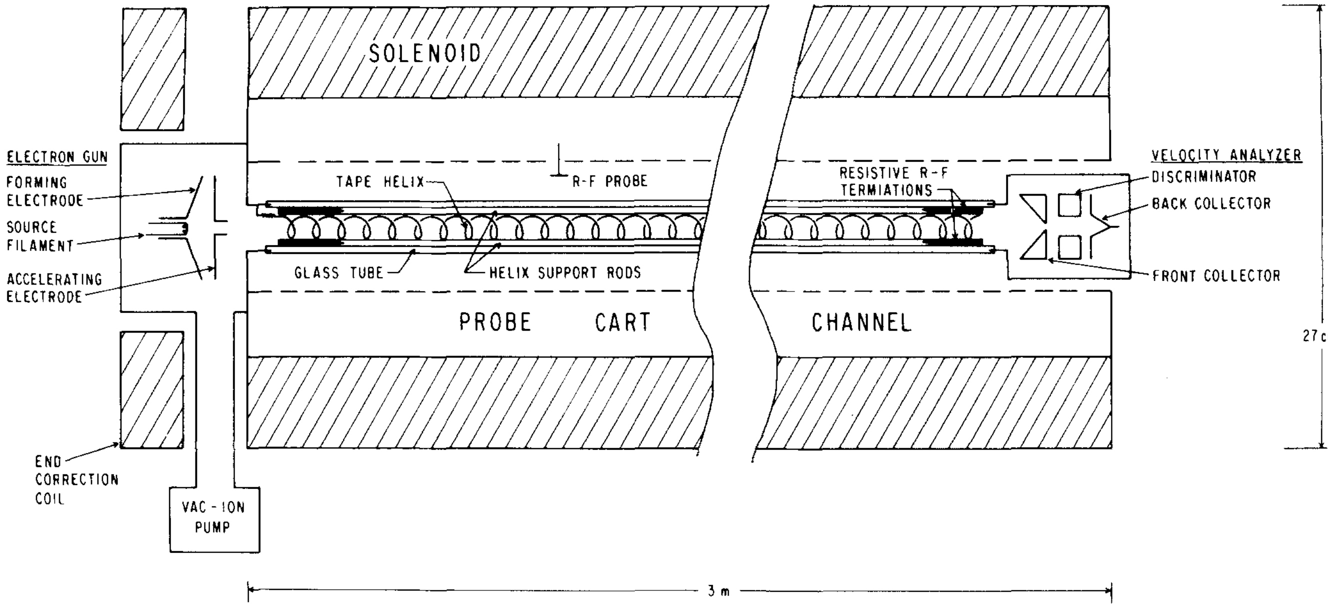

FIG. 1. Schematic diagram of traveling wave tube (not drawn to scale).

D. Method of solution

In order to solve Eqs. (17)–(20) and (31)–(34) we represent the beam by N charge sheets/wavelength and solve for the exact nonlinear dynamics numerically. We typically employ a total of 600 charge sheets. The equations are integrated with the Runge–Kutta method described by Hess[27] with a step size of $\Delta y = 0.01$. The linear solutions to the working equations form the entrance conditions for the numerical computations. The initial wave amplitudes are less than or equal to 0.03. We must specify the characteristic parameters C, b, and d for Eqs. (17)–(20) and b_j and d_j, $j = 0, \pm 1$ for Eqs. (31)–(34). Our numerical solutions agree with previously published results for the corresponding values of the characteristic parameters.

The integrity of the solutions to Eqs. (17)–(20) is monitored by integrating Eq. (22). We compute the integral

$$-2d\int_0^y A^2(y')\,dy' \tag{35}$$

and compare it to

$$\frac{1}{(1+Cb)}\int_0^{2\pi}\frac{d\phi_0}{2\pi}\,q(y,\phi_0)+A^2(y)\ . \tag{36}$$

The discrepancy remains smaller than 0.015 throughout a run of 2500 steps for finite damping. For $d=0$, it is less than 0.001.

III. EXPERIMENTAL APPARATUS AND LINEAR PROPERTIES

A. Experimental apparatus

When measured in wavelengths and total gain our traveling wave tube is 3–4 times longer than commercially available tubes. A schematic diagram is shown in Fig. 1. The principal parts are the electron gun, the slow wave structure including the probing system, the beam collector and analyzer, and the focusing solenoid.

The main element of the slow wave structure is BeCu tape (0.25 mm×1.25 mm) helix which has a length $L = 3$ m, an average radius $a = 8.06$ mm, and a pitch $p = 2.54$ mm. The pitch is maintained by three alumina rods which are epoxied to the helix 120° apart. This assembly is contained within a glass tubing (2.64 cm i.d. ×2.4 mm wall thickness) vacuum jacket which is centered on the axis of a conducting cylinder of radius 3.8 cm. The cylinder has four slots through which axially moveable electrostatic probes are inserted to transmit and recieve the electromagnetic waves.

Lossy resistive tapers terminate the helix at both ends. These imperfect impedance matches (voltage standing wave ratio $\simeq 1.1$) and variations along the slow wave structure reflect a small portion of the incident wave. The beating of the forward and reflected waves results in a small amplitude spatial oscillation of the measured wave power at $2k_{0r}$. However, the backward wave does not significantly affect the beam dynamics because it is far from synchronism with the wave.

The distributed loss k_{0i} can be varied by adding resistive strips which span the entire length of the tube. Adding these "attenuators" decreases the wavelength by less than 0.2%. The damping decrement k_{0i} is measured using wave transmission in the absence of the electron beam.

The electron beam source is a directly heated flat spiral filament of thoriated (1%) tungsten wire. The beam radius is $r_b = 3$ mm. It is confined on axis by a 440 G magnetic field which is uniform to ±1% in the interaction region. The beam is formed with apertured accelerating electrodes by immersed flow. We can vary the beam current and voltage in the range 0–30 mA and 0–3.8 kV.

A simple three-piece retarding field analyzer is used to both collect and velocity analyze the spent beam. The front collector allows 0.5% of the beam to pass. This is followed by an apertured discriminating electrode and back collector. We measure the beam power by integrating the current collected at the back collector versus the retarding voltage. We also measure the velocity distribution by electronically differentiating this signal. Prior to reaching the analyzer, the electrons drift through the helix termination region and their rf phases become confused. Consequently, we measure only the time-averaged velocity distribution. The analyzer position is fixed. However, the beam can be analyzed at different positions in the evolution of the instability by changing the position of the rf transmitter.

The wave power is measured continuously along the tube. A spectrum analyzer is used as a variable bandwidth detector. Broadband power measurements are made with a standard square-law detector. The probes are calibrated by measuring, with the velocity analyzer, the power lost by the beam when a single wave is excited. By equating the lost beam power to the wave power, we measure the probe coupling within an accuracy of ± 1 dB. The error is due to the small but finite dissipation ($k_{0i}/k_{0r} < 0.3\%$) and to wave reflections.

An interesting effect which occurs in a traveling wave tube and in the beam-plasma instability is the nonlinear wave phase shift. Since conventional interferometers have a limited spatial resolution, we use a special circuit to measure the wave phase continuously along z. The received rf signal is fed into the vertical input of an externally triggered sampling scope. The scope is operated in the external horizontal input mode. The time at which the rf signal is sampled following the scope triggering (sampling time) is determined by the output of a delya voltage generator. This generator simply steps its output voltage incrementally in the direction of the polarity of its input signal. Each voltage increment changes the sampling time by 1/1024 of the full horizontal time scale of the sampling scope. The verticle output of the sampling scope is connected to the delay voltage generator. The delay voltage adjusts automatically to lock onto a stable null, i.e., one with a negative slope, of the scope input signal. As the receiver probe moves a distance Δz, the scope triggers at a different rf phase of its input signal and the delay voltage for the tracked null V_n changes by $\Delta V_n \propto k_r(z)\,\Delta z$. Integrating from the transmitter position and electronically subtracting the linear phase $k_{0r}z$, we obtain the slowly varying phase

$$V_\phi(z) \propto \int_0^z [k_r(z') - k_{0r}]\,dz' \ . \qquad (37)$$

According to Eqs. (14) and (16) this can be expressed in terms of the scaled variables of the nonlinear theory as

$$\int_0^z [k_r(z') - k_{0r}]\,dz' = -[\theta(y) - by] \ , \qquad (38)$$

where we have neglected V_2 since $V_2 \ll V_1$ for small C. We call this the active wave phase because it is the slowly varying contribution to the wave phase which results from the presence of the beam. The left side is measured and the right side is computed in our numerical solutions.

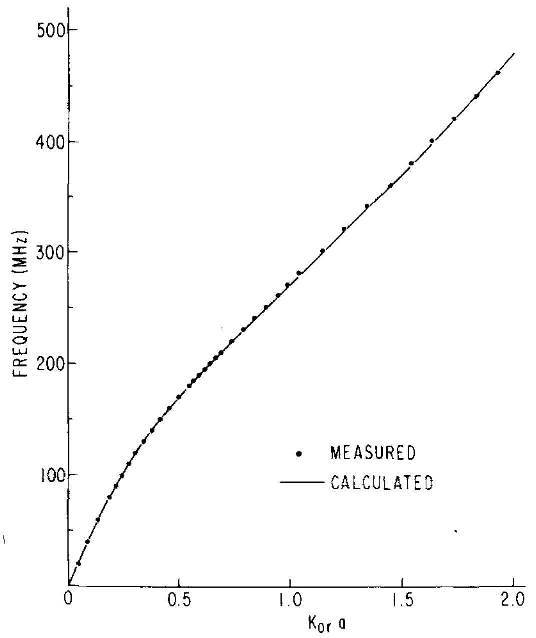

FIG. 2. Measured (points) and calculated (line) disperison relation for slow wave structure.

B. Dispersion properties

An electromagnetic wave on the helix can be thought of as propagating along the windings at nearly the speed of light. Consequently, the axial phase velocity is reduced by $p/2\pi a$. The dielectric supports also reduce the phase velocity slightly. The dispersion relation resembles that of a finite size plasma with a finite temperature.[5]

In Fig. 2 we compare the measured dispersion relation (points) with the theoretical prediction (line). The dispersion of the axisymmetric mode was calculated by solving Maxwell's equations across the waveguide area using two simplifying assumptions. First, we use the sheath helix model,[18] which assumes that the helix can be represented by an infinitely thin conducting cylinder in which the skin current is confined to flow in the direction of the windings. Second, we replace the three dielectric support rods by a uniform shell whose effective dielectric constant is the average $\epsilon_{eff} = 1 + 3(\epsilon_r - 1)A_r/A_s$, where $\epsilon_r = 8.6$ is the dielectric constant of the alumina rods and A_r is their cross-sectional area. The shell area, A_s, is the area of the region between the helix and the inner surface of the glass tube. The difference between the calculated and measured dispersion relation is less than 1% with no adjustable parameters.

C. Linear properties

In order to compare theory directly with experiment the characteristic parameters C, b, d, and QC must be known. We determine them experimentally be measuring the well understood linear properties of the traveling wave tube.[18,29]

The fundamental scaling parameter is Pierce's gain

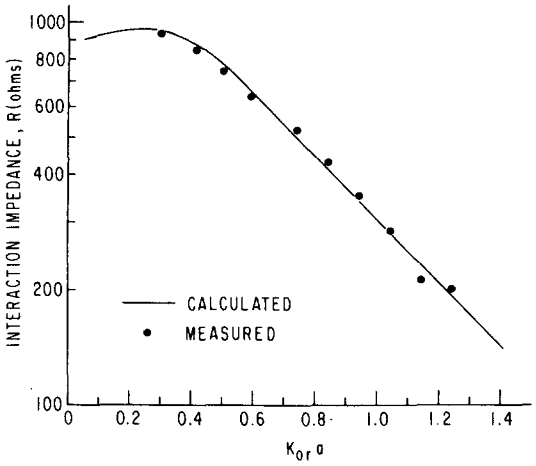

FIG. 3. Measured (points) and calculated (line) interaction impedance vs $k_{0r}a$ for our slow wave structure.

parameter C. To obtain C the interaction impedance R for our slow wave structure must be known. It can be calculated by using the radial eigenfunction we obtained while solving for the dispersion relation. The axial component of the normalized Poynting vector, $(\mathbf{E}\times\mathbf{B})_z/\langle E_z^2\rangle_b$ is integrated across the waveguide area to compute R from Eq. (1). Space harmonics due to the periodicity of the helix are accounted for in the manner described by Tien.[30] The result of this calculation is shown by the line in Fig. 3. The interaction impedance decreases dramatically as $k_{0r}a$ increases because the radial eigenfunction, in particular E_z, becomes concentrated near the helix away from the beam for large $k_{0r}a$.

The interaction impedance is obtained experimentally by using the Kompfner dip.[20] Launching a small monochromatic signal with a point source establishes three waves, i.e., one helix and two beam modes, each with a different phase velocity. For $C \ll 1$, these modes remain of comparable amplitude and can interfere destructively to yield a null signal at some distance Z_K downstream from the transmitter. This null is known as the Kompfner dip. The conditions for its occurence are

$$\omega C Z_K/2\pi u_0 = g_1(d, QC) \ , \tag{39}$$

and

$$(k_{0r} - \omega/u_0)\, Z_K = g_2(d, QC) \ , \tag{40}$$

where g_1 and g_2, which are calculated by Johnson,[31] are weak functions of d and QC for small d and QC. By measuring k_0, I_0, V_0, and Z_K, one can solve Eq. (39) to determine R at each frequency. For the weak beams employed in these measurements QC was negligible in Eqs. (39) and (40). The measured values of R are the points in Fig. 3 and they agree to within ± 6% of the calculated values. Since ω and k_0 are measured independently, Eq. (40) can be used to obtain the beam drift velocity u_0. This measurement yields u_0 to within 0.5% of that measured with the velocity analyzer.

The experimentally determined interaction impedance is combined with measurements of I_0 and V_0 to compute C according to Eq. (3). With the measured values of u_0 and $v_{ph} = \omega/k_{0r}$, we obtain b according to Eq. (5) to within $b = \pm 0.2$. The damping decrement k_{0i}, measured in the absence of the beam, is used to determine d according to Eq. (6).

The remaining unknown parameter is QC. It can be determined from measurements of the linear growth rates over the instability bandwidth.[29] Since I_0, u_0, and r_b are measured with the velocity analyzer, ω_{pb} is known and the only unknown quantity in Eq. (4) is the finite size reduction factor R_q. In general, it is a complicated function of many parameters, but it can be approximated by[32]

$$R_q \simeq [1 + (\gamma u_0/\omega r_b)^2]^{-1/2} \ , \tag{41}$$

where γ is an unknown geometrical constant.

To determine γ, we plot the normalized linear growth rate versus b in Fig. 4. The points are measurements at wave frequencies ranging from 80 MHz to 260 MHz for $I_0 = 10$ mA and $V_0 = 920$ V. The curves are computed in the following way: Measured quantities are used to obtain QC at each frequency according to Eqs. (4) and (41) with γ as a free parameter. We then insert QC and the experimentally determined values of C, b, and d into Eq. (8) and solve it numerically for δ. The only adjustable parameter γ is varied to obtain agreement between the measured and calculated growth rates. The best visual fit occurs for $\gamma = 1.0 \pm 0.1$. This yields a reduction factor which agrees with calculated values[25] for a constant density beam in a conducting tube of radius $3r_b$. The same value γ is obtained for many beam currents and voltages.

The role of QC in determing which wave grows the fastest is illustrated by the data in Fig. 4. It is near the intersection of the unperturbed slow branch of the beam dispersion and the helix dispersion relation, i.e., $b \simeq (4QC)^{1/2}$. This is satisfied at $b = 0.85$ where we calculate $QC = 0.19$.

IV. NONLINEAR PROPERTIES

The spatial evolution of a single launched wave in the presence of a strong beam is shown in Fig. 5. The

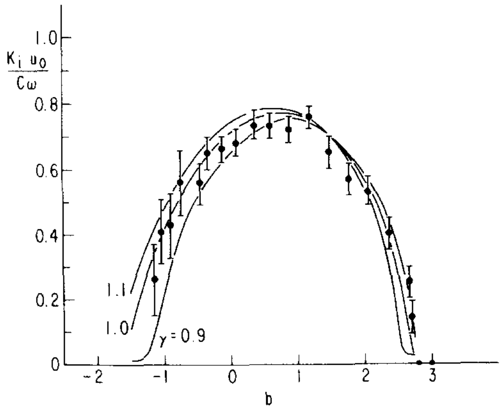

FIG. 4. Normalized growth rate $k_i u_0/C\omega$ vs the detuning parameter b. Points are measured. Lines are calculated with γ as free parameter. Best fit occurs for $\gamma = 1.0 \pm 0.1$.

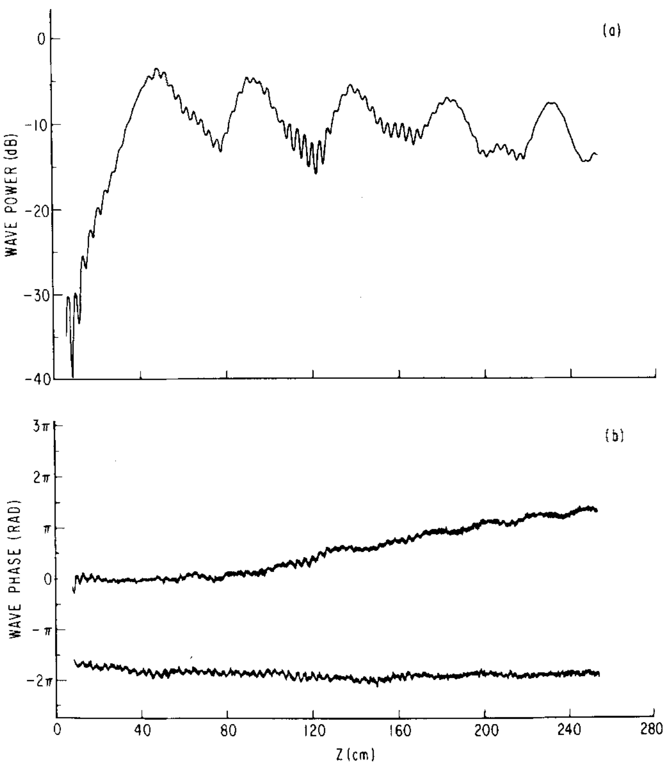

FIG. 5. (a) Wave power normalized to the injected beam power vs distance from the transmitter, (b) Active wave phase vs z. Baseline is measured in absence of beam. $\omega/2\pi = 220$ MHz, $I_0 = 30$ mA, $V_0 = 1$ kV. From linear measurements these correspond to $C = 0.15$, $b = 1.6$, $d = 0.025$, and $QC = 0.32$.

wave power is normalized to the injected beam power and plotted versus the distance from the transmitter. The power grows by a factor of 10^3 to saturation and then executes five trapped particle oscillations. This contrasts the typical behavior in beam-plasma systems where the wave decays away rapidly following the first oscillation. In this case, the wave power at the peak of the oscillations decreases by 4 dB from saturation to the end of the interaction region because of the finite dissipation in the slow wave structure. Over the same distance the bounce length increases by only 10%. As previously described, the fast oscillations at $2k_{0r}$ are a result of wave reflections. The frequency spectrum, measured in the range 1–500 MHz, is dominated by the fundamental mode and its first harmonic. Unstable noise grows in the nonlinear region, but it is still 40 dB below the main wave power level at $z = 240$ cm.

Figure 5(b) is the active wave phase [defined by Eq. (38)] plotted as a function of position. The measurement technique is described in Sec. IIIA. In the absence of the beam we obtain the almost straight baseline. With the beam, the phase departs from linearity near the position where the wave power saturates because the phase velocity of the wave decreases. The wave slows down in the nonlinear region to accommodate the beam particles, which decelerate in the laboratory frame as they transfer energy to the wave. The average slope of the wave phase following saturation yields $\langle \delta k_{nl} \rangle = 0.021$ cm^{-1}. For $C = 0.15$, $b = 1.5$, and $d = 0.03$ the numerical solution predicts $\langle \delta k_{nl} \rangle = 0.020$ cm^{-1}. Careful inspection of the wave phase in the nonlinear region reveals that the slope, i.e., δk, oscillates at $2k_b = 4\pi/\lambda_b$, where λ_b is the bounce length. This agrees with theory and follows from Eq. (23) since q^2 oscillates at twice the rate that A^2 does. Similar δk oscillations have been predicted[33] and observed[34] for large amplitude plasma waves.

The amplitude oscillations occur because the particles are sloshing back and forth in the wave trough. However, the phase oscillations reveal that the wave potential oscillates under the particles as well. These variations in the wave amplitude and phase have important consequences with regard to the stability of the trapped particle equilibrium. They also modify the relationship between the bounce length and the wave amplitude. We shall elaborate on these points in the following sections.

The normalized wave power at the initial saturation point is plotted vs C in Fig. 6. The line represents our calculations for $b = 1.0$ and $d = 0$. To obtain the experimental points the beam voltage was held constant while the current was varied to change C. Since the saturation power is sensitive to the detuning, the wave frequency was adjusted at each point to keep $b = 1.0$. Under these conditions, the space charge parameter increases when the beam current is increased. For small C the experimental points agree with the calculations. As C increases, the agreement deteriorates because the beam space charge, which is neglected in the calculations, becomes important. The results in Fig. 6 are consistent with previous measurements[21] of the saturation power. As in the beam-plasma instability, the saturation power is indeed proportional to CI_0V_0 for small C. However, this is relaxed for strong beams by the large decrease in the particle velocity and the beam space charge.

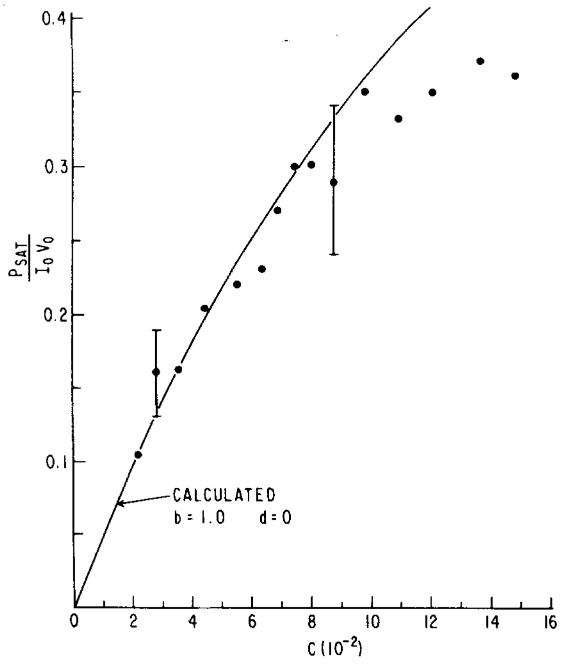

FIG. 6. Wave saturation power normlaized to the injected beam power vs C. For measured points the detuning was held constant at $b = 1.0$. Line computed with $b = 1.0$ and $d = 0$.

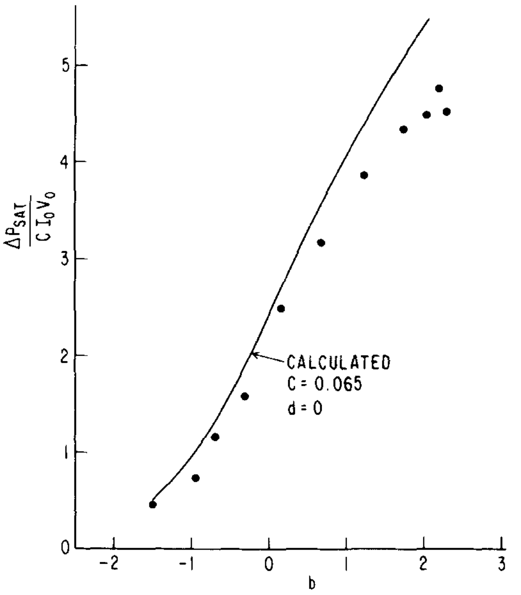

FIG. 7. Lost beam power at saturation normalized to CI_0V_0 vs detuning parameter b. Points taken for $I_0 = 1.25$ mA and $V_0 = 902$ V. Detuning varied by changing frequency. Line calculated with $C = 0.065$ and $d = 0$.

The dependence of the saturation power on the detuning is shown in Fig. 7. The detuning parameter b was varied experimentally by changing the frequency while the beam current and voltage were kept constant. Since C varies slightly with frequency, the saturation power is normalized to CI_0V_0 to facilitate comparison between theory and experiment. For the experimental points, C varied by 10% about its average of 0.065. The line corresponds to our calculation for $C = 0.065$, $d = 0$. The measurements agree with theory within the experimental error. That the saturation power increases with b can be understood qualitatively from the trapping model. The difference between the beam injection velocity and the linear phase velocity of the unstable wave Δv increases with b. Strictly speaking, the wave saturates when the net energy exchange between the electrons and the wave becomes zero. According to the trapping model, this occurs near the bottom of the electron vortex motion in phase space, which corresponds roughly to a decrease of $2\Delta v$ in the beam velocity. Since the wave gains the power lost by the beam, the wave saturation power increases accordingly. This simple model neglects finite beam strength effects, i.e., finite C and QC, but still gives the correct qualitative behavior.

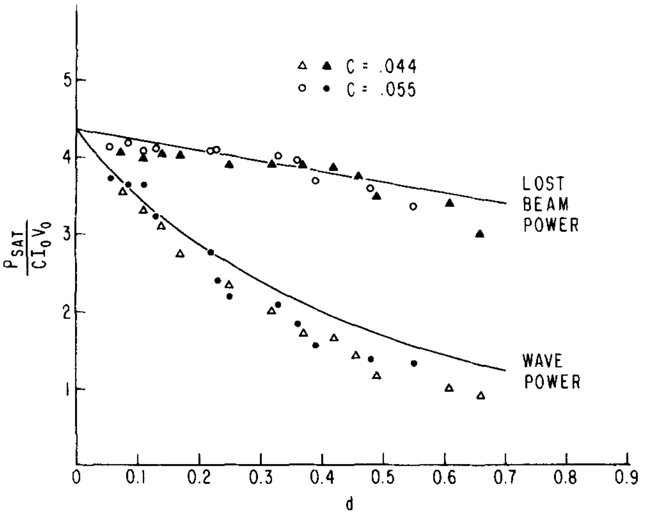

FIG. 8. Lost beam power and wave power (both at saturation) vs damping coefficient d. Points are measured for $I_0 = 0.4$ mA ($C = 0.044$) and 0.8 mA ($C = 0.055$) and $V_0 = 920$ V with frequency chosen to set $b = 1.0$. Lines computed with $b = 1.0$ and $C = 0.05$.

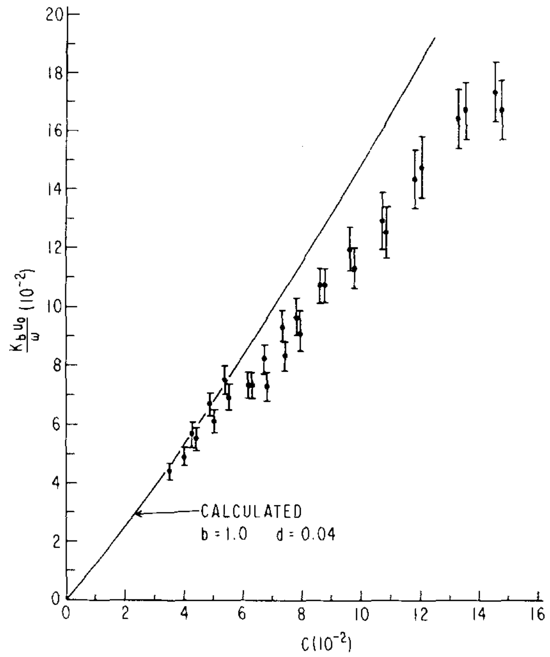

FIG. 9. Normalized bounce wavenumber $k_b u_0/\omega$ for first trapping oscillation vs C. Measured points taken with $b = 1.0$. Line computed with $b = 1.0$ and $d = 0.04$.

Figure 8 shows the effect of damping on the saturation power. The damping rate is varied by means of the attenuators described in Sec. III. The saturation wave power is measured with a calibrated probe. The difference between the injected beam power and the beam power at saturation (lost beam power) is measured with the velocity analyzer. Both quantities are normalized to CI_0V_0. The data were taken at two beam currents at a constant voltage such that $C = 0.044$ and 0.055, with the frequency chosen to set $b = 1.0$. The lines are the theoretical predictions for $b = 1.0$ and $C = 0.05$. They agree with the measurements within the experimental error. It is not surprising that damping dissipates wave power in proportion to d. However, these data indicate the dynamic role of wave damping in this instability. Prior to saturation, the wave is on average a decelerating force on the beam. This is evident because the wave grows at the expense of the beam. When the damping is increased, the wave amplitude is generally smaller throughout the growth region. The average decelerating force is reduced and, as a result, the wave extracts less energy from the beam. Consequently, the lost beam power at saturation decreases as d increases.

We plot the normalized bounce wavenumber $k_b u_0/\omega$ vs C in Fig. 9. The detuning parameter is kept constant at

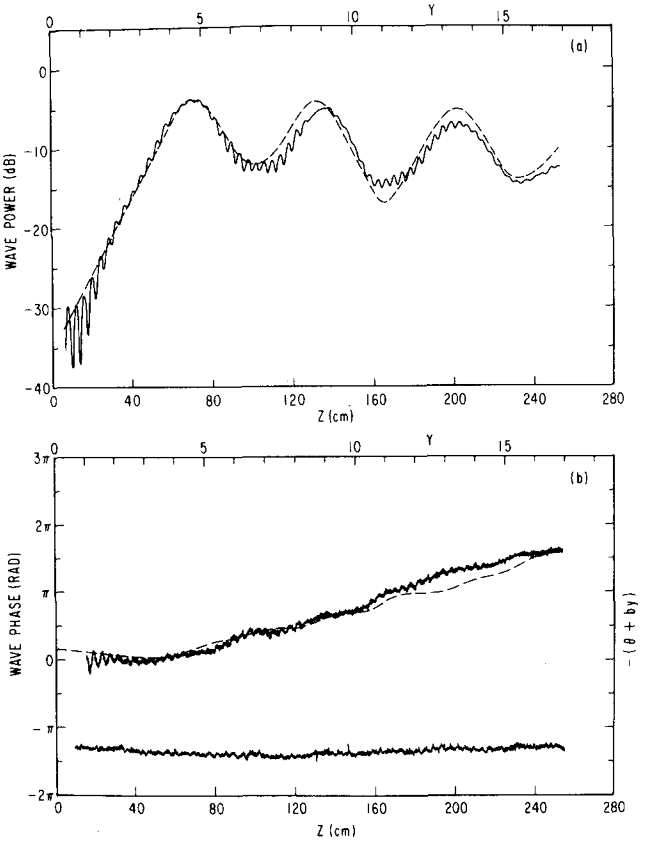

FIG. 10. (a) Wave power normalized to injected beam power vs distance. (b) Active wave phase vs distance. Solid lines are measured with $\omega/2\pi = 195$ MHz, $I_0 = 11$ mA, $V_0 = 960$ V corresponding to $C = 0.12$, $b = 1.2$, $d = 0.033$, and $QC = 0.2$. They are plotted vs z. Dashed lines computed with $C = 0.12$, $b = 1.0$, and $d = 0.03$. They are plotted vs y.

$b = 1.0$. According to theory $k_b u_0/\omega = 2\pi C/y_b$ is the distance between amplitude maxima in the computations. It is a function of the characteristic parameters and varies as the instability evolves for $d \neq 0$. The calculated result for the first bounce length for $b = 1.0$ and $d = 0.04$ is represented by the line in Fig. 9. It agrees with the measurements for $C \lesssim 0.06$. For larger values of C the theory predicts shorter bounce lengths than observed by 20%. We believe this decrepancy is due to our neglect of the space charge force in the calculations.[27]

The basic results of this section are (1) that the trapping oscillations can persist for many bounces and (2) the theory accurately describes the nonlinear behavior of the instability. This provides the basis for studying the stability of the trapped particle state.

V. WAVE DAMPING

The trapping oscillations of a single wave can be destroyed through dissipation in the slow wave structure. The details of the nonlinear evolution of the instability in the presence of damping vary for different values of the characteristic parameters, in particular, the damping coefficient d. However, the detrapping process itself remains basically the same over a wide range of values of C, b, and d. In this section, we investigate the basic detrapping mechanism caused by the circuit damping.

For reference, Fig. 10 shows three trapping oscillations when the damping rate is very small, i.e., $k_{0i} = 2.7 \times 10^{-3}$ cm^{-1}. The solid line in Fig. 10(a) is the measured power of a single launched wave vs z (indicated across the bottom of the figure). The characteristic parameters are $C = 0.12$, $b = 1.2$, and $d = 0.033$. The dashed line is the calculated power vs y (indicated across the top of the figure) for $C = 0.12$, $b = 1.0$, and $d = 0.03$. The theoretical wave power is computed with the numerically obtained $A(y)$ according to Eq. (21) and agrees within ± 2 dB in absolute magnitude with the measured wave power. The y axis had to be rescaled with respect to z in order to obtain the best spatial fit. In absolute terms, the distances predicted by $z = u_0 y/C\omega$ were 17% shorter than those measured. For example, the predicted distance between the first and third peak is $u_0 \Delta y_{13}/C\omega = 110$ cm while the measured distance is $\Delta z_{13} = 132$ cm. As in Fig. 9, we believe this discrepancy is due to neglect of the beam space charge in the nonlinear calculations.

The solid line in Fig. 10(b) is the measured active wave phase vs z. Once again the phase velocity decreases in the nonlinear region and oscillates at $2k_b$. The average slope yields a wavenumber shift of $\langle \delta k_{n1} \rangle = 0.026$ cm^{-1}. The dashed line is the calculated phase $-(\theta + by)$ plotted vs y.

Figure 11 shows the development of the instability

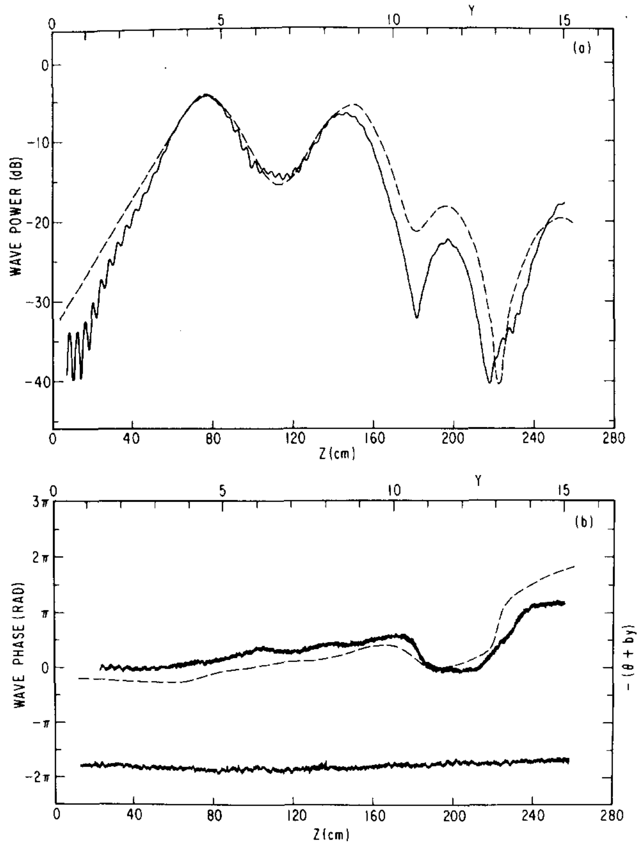

FIG. 11. (a) Wave power normalized to injected beam power vs distance. (b) Active wave phase vs distance. Measurements (solid lines) have same characteristic parameters as in Fig. 10 except the damping is increased to $d = 0.082$. Calculations (dashed lines) gives best fit for $C = 0.12$, $b = 1.0$, and $d = 0.078$.

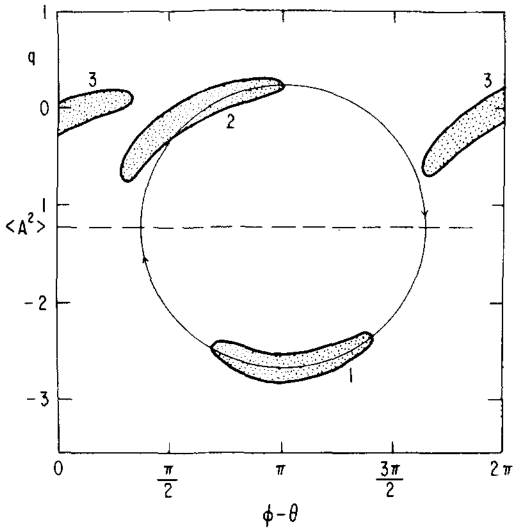

FIG. 12. Schematic of phase space distribution at three positions in a trapping oscillation with damping. The abscissa is the particle phase in the instantaneous wave frame.

when the damping rate is increased to $k_{0i} = 6.6\times10^{-3}$ cm^{-1} ($d = 0.082$) by adding attenuation as described in Sec. III. All other parameters are identical to those in Fig. 10. Prior to the second peak, the additional damping does not significantly alter the spatial evolution of the wave. However, following the second maximum the power falls dramatically and fails to regrow to the previous large level. At the deep power minimum at $z = 180$ cm the wave undergoes a rapid phase shift, shown in Fig. 11(b), of 1.9 rad over a distance of 10 cm, which corresponds to $\Delta k/k_{0r} = -25\%$. At the following power minimum the phase shift is 3.6 rad over 22 cm, which corresponds to $\Delta k/k_{0r} = +21\%$.

The dashed lines in Fig. 11 are the computed wave amplitude and phase plotted vs y for $C = 0.12$, $b = 1.0$, and $d = 0.078$. These values of the characteristic parameters give the best agreement with the measurements and are within the experimental error of the values inferred from linear measurements. As in Fig. 10, the y axis was rescaled with respect to z to obtain the best spatial fit. In absolute terms, the predicted distances are 26% shorter than those measured. (This renormalization is responsible for most of the discrepancy in the linear growth rate.) Nevertheless, the numerical solutions reproduce the essential features of the experimental results. Following the second maximum the trapping oscillations are dramatically altered; the wave experiences very deep power minima and large phase shifts.

As a result of our computer studies, we can explain the salient features in Fig. 11 by tracing the motion of the particles in phase space. We indicate the motion schematically in Fig. 12 to accentuate the main points. Instead of plotting just the particle phase ϕ, the abscissa, is the particle phase in the instantaneous frame of the wave $\phi-\theta$ because, according to Eq. (20), this is the phase which determines the force. This is an important point because the wave phase shifts $\Delta\theta$ move the potential with respect to the particles and affect their acceleration. The potential minimum is at $\phi-\theta=\pi$. The ordinate is the scaled particle velocity. At the second power maximum in Fig. 11, the bulk of the particles are at the bottom of their phase space orbit, denoted by the shaded region 1, and are moving into the accelerating region $0 < \phi-\theta < \pi$. While they are accelerated, the particles regain momentum (energy in the laboratory frame) at the expense of the wave. However, since it has been attenuated, the wave is energetically incapable of forcing the particles out of the accelerating region before vanishing. For example, the particles may reach position 2 as the wave amplitude approaches zero. At this point, the wave shifts its phase θ so as to transfer the majority of the particles into the decelerating region of the wave potential, e.g., position 3. The wave now extracts energy from the particles on the average and regrows. Since they have finite spread in phase, not all particles reach the decelerating region as a result of the wave shift. Some remain within the accelerating region as shown at position 3. In cases where the particles being decelerated only slightly outnumber those being accelerated, the subsequent net energy exchange between the wave and particles is small. Consequently, the peak wave power levels following these phase shifts will be relatively low, as shown in Fig. 11.

That the phase shifts tend to move the particles from the accelerating region toward the decelerating region of the wave potential can be seen by inspecting Eq. (18). For simplicity, assume that the particles are tightly bunched at a single phase $\chi\equiv\phi-\theta$ and that $C \ll 1$. For phase shifts which occur rapidly enough to ignore particle velocities, the predominant change in the clump phase is given by Eq. (18)

$$\Delta\chi \simeq -\Delta\theta \simeq -\int_y^{y+\Delta y} \frac{\cos\chi}{A}\, dy' . \qquad (42)$$

The sign of $\Delta\chi$ is determined by $-\cos\chi$, which has a positive slope at the zero $\chi=\pi/2$ and a negative slope at the zero $\chi = 3\pi/2$. Consequently, the phase shifts tend to transfer the clump away from the unstable node $\chi = \pi/2$ toward the stable node $\chi = 3\pi/2$, which lies in the decelerating region of the wave potential. If the particle clump has a finite spread in phase space, the analysis becomes complicated. However, our numerical studies indicate that the phase shifts remain a survival mechanism for the wave.

The large and rapid phase shifts occur when the amplitude decreases to

$$A < \left| \int_0^{2\pi} \cos(\phi-\theta)\, \frac{d\phi_0}{2\pi} \right| , \qquad (43)$$

which can be quite small if most of the particles are near the unstable node. In this case, shifts of order $\pm\pi$ can occur since the clump originates near $\pi/2$ and stops at $3\pi/2$. The $\pm$ sign depends on which side of $\pi/2$ the move originated. This is illustrated nicely in Fig. 11(b). The phase shift at the second minimum is $\Delta\theta_2 = -1.9$ rad and $\Delta\theta_3 = 3.6$ rad at the third. The larger phase shift occurs at the deeper minimum and has the opposite sign.

The particle phase mixing is evident in Fig. 13,

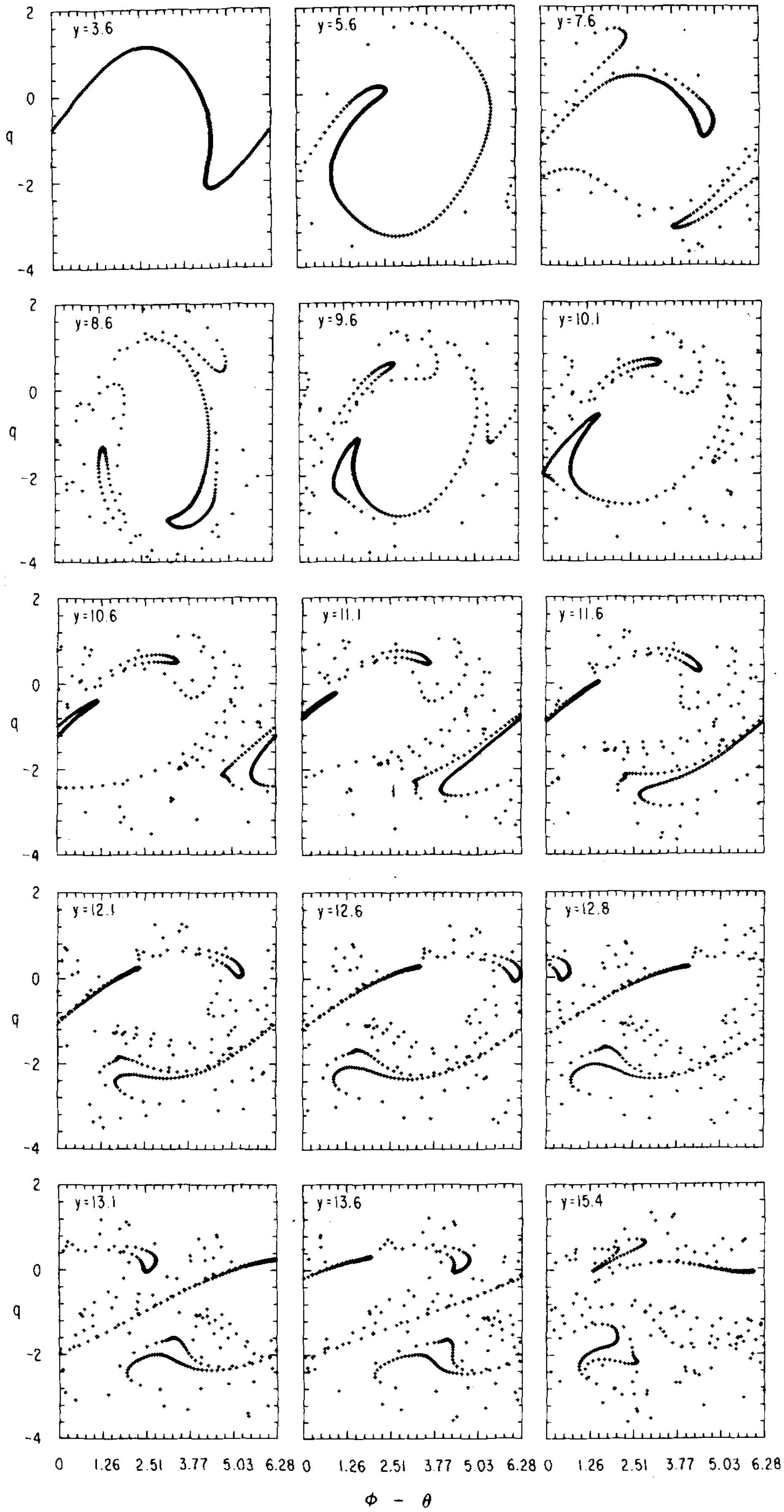

FIG. 13. Phase space dynamics at various positions y for the calculation in Fig. 11. The abscissa is the particle phase in the instantaneous wave frame.

where we show the spatial development of phase space for the computation in Fig. 11. As in Fig. 12, the abscissa is the particle phase in the instantaneous wave frame $\phi - \theta$ because this is the phase that determines the force. As a result of the reduced amplitude and phase shifts, particles spill into adjacent wave troughs. Prior to the second amplitude peak near $y = 8.6$, only an insignificant number of particles in the filamentary tail are affected. However, at the first deep amplitude minimum near $y = 10.1$, the wave shifts its phase and transfers the clump to the potential maximum at $\phi - \theta = 0$; there the clump is broken in half. There are nearly as many particles being accelerated as there are being decelerated. Consequently, little net energy exchange will occur and the wave will remain at a relatively low power level. Another phase shift follows at the next amplitude minimum near $y = 12.6$ to increase the spillage. The spilled particles rotate out of synchronism with the unspilled particles and, in general, along different phase trajectories. Since the bounce frequency depends on their oscillatory energy,[35] the particles rotate at different rates and eventually phase mix.

The phase average velocity distribution, near the position of the last power maximum in Fig. 11, is shown in Fig. 14. The histogram is computed at $y = 15.3$ and the curve is measured at $z = 265$ cm. The basic characteristic is the double peak within a velocity spread of the trapping width $\Delta u = \pm 2Cu_0 = \pm 0.24u_0$. Nearly half of the particles have a velocity near the injection velocity, with some actually moving faster than at injection. This distribution may lead to further instability, but we have not yet investigated the next stage in its development. By $z = 265$ cm, 19% of the injected beam power, or roughly half of the wave saturation power, has been dissipated through wave damping. This agrees with the predicted value of 18%.

To demonstrate that this detrapping process is due to just a single wave, we show the spatial evolution of the frequency spectrum in Fig. 15. Near the first deep minimum, the noise is more than 60 dB below the main wave power level. As the instability progresses, sidebands characteristic of a trapped particle instability develop. The upper sidebands achieve larger amplitudes because they are resonant with the slowed beam. By $z = 250$ cm these sidebands have attained a power level 60 dB below the saturation power. According to our sideband experiments, this is orders of magnitude below the level at which sidebands cause detrapping. This detrapping process is indeed single wave although the subsequent development may be affected by the sidebands.

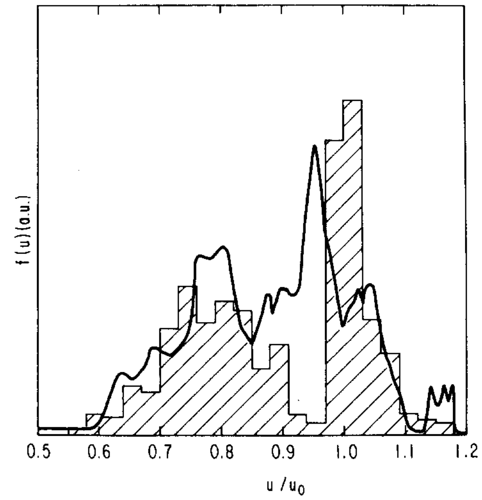

FIG. 14. Phase averaged velocity distribution vs velocity normalized to the injection velocity. Solid line is measured at $z = 260$ cm in Fig. 11. Histogram is computed result at $y = 15.3$.

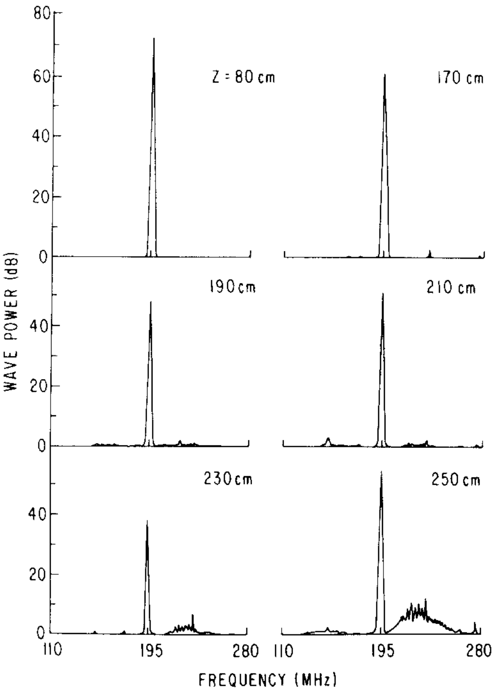

FIG. 15. Measured frequency spectrum at various positions in Fig. 11.

Figure 11 demonstrates that a small damping rate, $k_{0i}/k_{0r} \sim 0.08$ C (= 0.01 in our example) can have a catastrophic effect on the trapping oscillations. We expect a similar behavior in beam-plasma systems. However, one must be careful in applying our result if the damping mechanism is some form of Landau damping. The saturated wave alters the plasma distribution near the phase velocity of the wave by capturing the resonant particles. Therefore, the linear Landau damping rate in the absence of the beam does not apply in the nonlinear region. However, there are damping mechanisms which do apply in the nonlinear beam-plasma instability, such as, (1) collisional wave damping and (2) an effective damping of the saturated wave through nonlinear decay processes. In these cases, we would expect a behavior similar to that describe here.

VI. EFFECT OF WAVE PHASE SHIFT IN BOUNCE LENGTH

The nonlinear wave phase shifts alter the relation between the bounce length and the wave amplitude, which is usually found to be[35] $k_b \sim \omega_b/u_0 \sim (ek_0E/mu_0^2)^{1/2}$. However, in obtaining this result, the ability of the wave to change its phase velocity is neglected. According to Eq. (20), the force on a particle depends on its phase in the instantaneous wave frame $\phi - \theta$. However, wave phase shifts can alter the force by shifting the potential with respect to the particles. The effect this has on the bounce length can easily be determined for a single macro-particle which is trapped in a traveling wave. The self-consistent equations for this interaction can be derived by simply assuming that the beam particles are premodulated and enter the interaction region at a single phase $\chi \equiv \phi - \theta$. Then for $C \ll 1$, Eqs. (17)-(20) become

$$dA/dy = -\sin\chi - dA \ , \tag{44}$$

$$d\theta/dy = \cos(\chi)/A - b \ , \tag{45}$$

$$d\phi/dy = q \ , \tag{46}$$

$$dq/dy = 2A\sin\chi \ , \tag{47}$$

where the subscript j has been dropped. For simplicity, assume that $d \ll 1$, and the particles are deeply trapped such that $\delta\chi \equiv \chi - \pi \ll 1$. By applying these approximations to Eqs. (44)-(47), we obtain the equation of motion in the instantaneous wave frame to $O(\delta\chi)$

$$\frac{d^2\delta\chi}{dy^2} = \frac{d^2\phi}{dy^2} - \frac{d^2\theta}{dy^2} \simeq -2A\delta\chi - \frac{\delta\chi}{A^2} \ . \tag{48}$$

The first term on the right-hand side is the ordinary restoring force at the bottom of the wave potential. The second term is an "inertial force" which results from the wave phase shifts. Notice that, for this deeply trapped particle, it is a restoring force whose magnitude is proportional to the displacement of the particle from the bottom of the potential well and inversely proportional to the square of the wave amplitude. This term becomes appreciable at small amplitudes; remember the large phase shifts in Fig. 11 occurred at power minima. Solving Eq. (48) we find

$$\kappa_b = 2\pi/y_b = (2A_0 + A_0^{-2})^{1/2} \ , \tag{49}$$

where A_0 is the normalized wave amplitude averaged over a bounce length. This relation is independent of b. For large amplitudes, the phase shifts are unimportant and we obtain the usual result, $\kappa_b \simeq (2A_0)^{1/2}$. For $A_0 \ll 1$, the inertial force dominates and we obtain $\kappa_b \simeq 1/A_0$, i.e., the bounce length increases with amplitude.

We have also solved Eqs. (44)-(47) numerically using the method described in Sec. II. The result of a representative run is denoted by the dots in Fig. 16. The ordinate is the scaled distance y_b that the macro-particle travels in the laboratory frame while it executes one complete rotation in phase space. For small damping rates this corresponds to the distance between successive amplitude maxima. The value of A_0 for each point is calculated by averaging the solution $A(y)$ over the corresponding y_b. As the solution progresses in y the amplitude decreases due to damping and the bounce length changes accordingly. The particle remains trapped throughout. The computed points agree to within 5% with our approximate analytical solution.

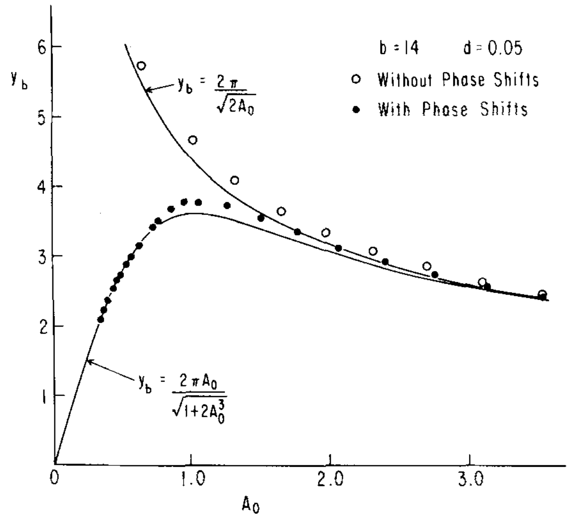

FIG. 16. Normalized bounce length vs wave amplitude (averaged over bounce length). Lines are analytical results with and without the wave phase shifts. Solid points are from numerical solutions to Eqs. (44)-(47). Open circles are computed with $\cos(\chi)/A$ term in Eq. (45) omitted.

In this example, $\delta\chi_{\max} \simeq 0.9$, which means that the particle samples the nonlinearity in the sinusoidal electric field. This is the source of the small discrepancy. Numerical solutions for various values of b, d and initial conditions give similar agreement.

In the case of many particles the analysis becomes complicated. However, the data in Fig. 11 support the result found here. The distance between the second and third and the third and fourth power maxima are both shorter than the first bounce length even though the amplitude is far smaller. We attribute this to the large wave phase shifts. Under less dramatic conditions, the phase shifts are not as pronounced and merely regulate the bounce length. For example, the bounce length in Fig. 5 increased by only 10% while the wave amplitude decreased by 40% over the same distance.

VII. MANY WAVE EXPERIMENT

The trapping oscillations of the saturated wave can also be destroyed by launching waves at neighboring frequencies. This is illustrated in Fig. 17. The dashed line in Fig. 17(a) is the total wave power when we launch only the main wave at $\omega_0/2\pi = 183.5$ MHz. It undergoes three trapping oscillations while the peak wave power falls by 3 dB due to the finite circuit damping. The solid line is the total wave power when we launch the main wave and a smaller amplitude (by 11 dB) wave at $\omega_{+1}/2\pi = 220.2$ MHz ($\omega_{+1} = 6\omega_0/5$). The presence of the additional wave destroys the trapping oscillations near the second minimum. When we increase the initial amplitude of ω_{+1}, the oscillations are destroyed earlier. Since the two curves in Fig. 17(a) do not begin to separate until the second maximum, the disruption occurs over a short distance, i.e., a fraction of a bounce length. Following the destruction, the power remains farily constant at a level significantly below the power maxima. Most of the available wave power has returned to the beam.

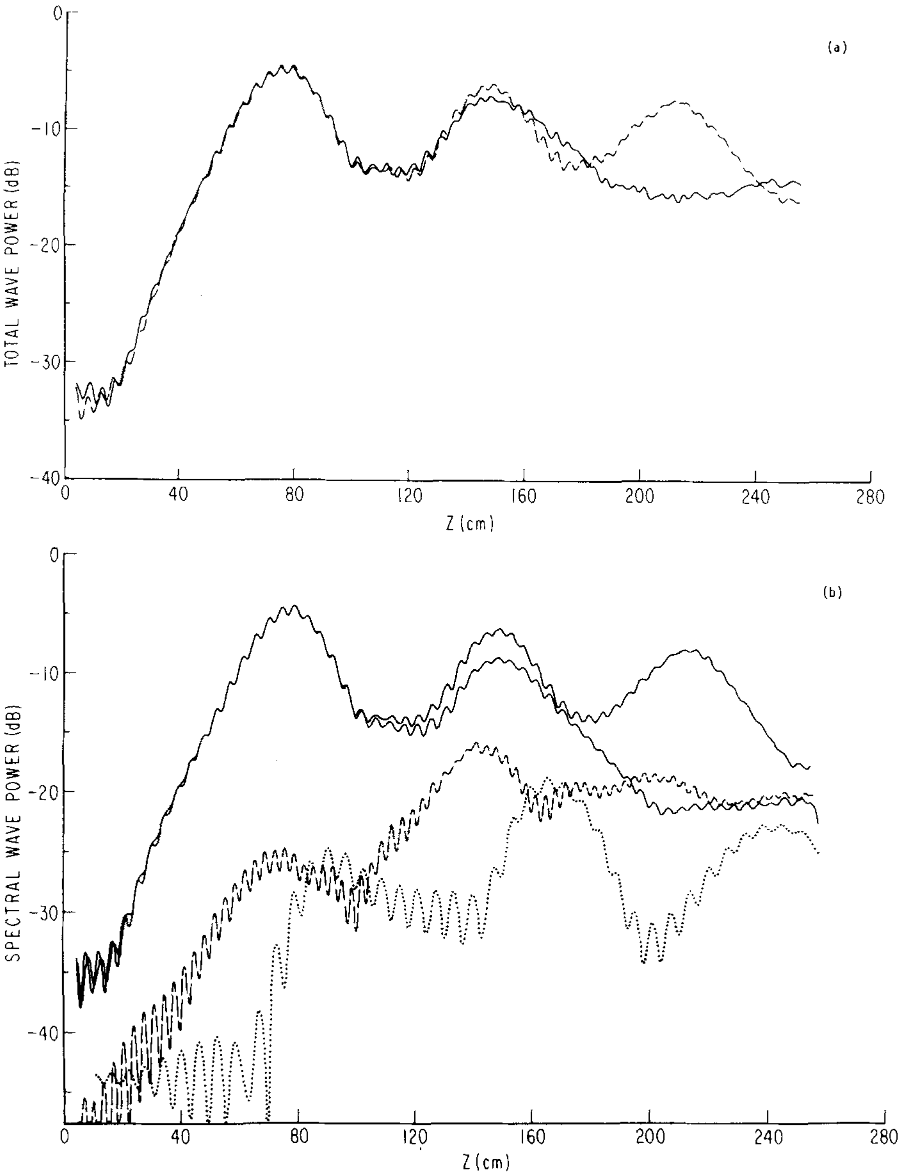

FIG. 17. (a) Total wave power (1–400 MHz) normalized to injected beam power vs distance. Dashed curve: launch $\omega_0/2\pi = 183.5$ MHz only. Solid curve: launch $\omega_{+1}/2\pi = 220.2$ MHz at low level in addition to ω_0. (b) Wave power of dominant spectral components (1 MHz bandwidth). For main wave (solid line) $C = 0.12$, $b_0 = 0.8$, $d = 0.032$. For upper sideband (dashed line) $C = 0.11$, $b_{+1} = 1.8$, $d_{+1} = 0.032$. For nonlinear image wave (dotted line) $\omega_{-1}/2\pi = 146.8$ MHz, $C = 0.13$, $b_{-1} = 0.2$, $d_{-1} = 0.025$. $I_0 = 9.6$ mA and $V_0 = 940$ V.

The behavior of the dominant spectral components is shown in Fig. 17(b). The upper solid line is the main wave when we launch it alone. The lower solid line is the main wave when we launch both ω_0 and ω_{+1}. The linearly unstable wave ω_{+1} (dashed line) continues to grow in the nonlinear region until the trapping oscillations are destroyed near the second minimum. The dotted line is the nonlinear product at 146.8 MHz. It grows dramatically when the dynamics become nonlinear, namely, within the last e folding before saturation.

Of course, other nonlinear products[36] appear at frequencies $\omega_n = \omega_0 + n\Delta\omega$, where $\Delta\omega = \omega_{+1} - \omega_0$ and $n = \pm 1, \pm 2, \ldots$. Frequency spectra at various positions are shown in Fig. 18. Prior to the destruction, the dominant modes are ω_0, ω_{+1}, and ω_{-1}. However, some higher order products grow in the nonlinear region. They finally attain amplitudes comparable to that of the main wave near the end of the tube.

Since the dynamics prior to the destruction are dominated by only three waves whose phases are not random,

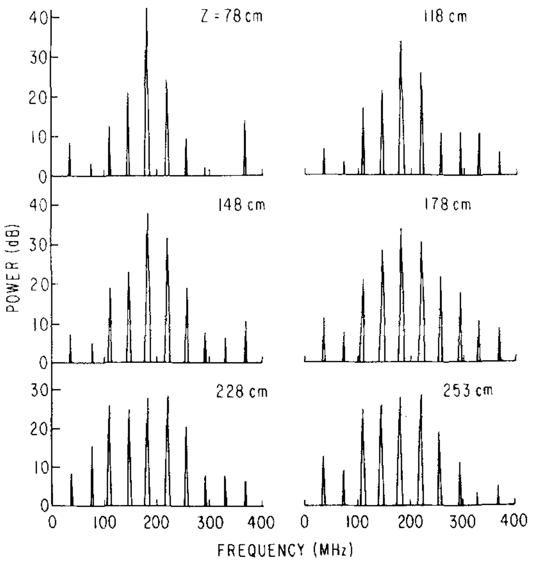

FIG. 18. Measured frequency spectrum at six positions in Fig. 17.

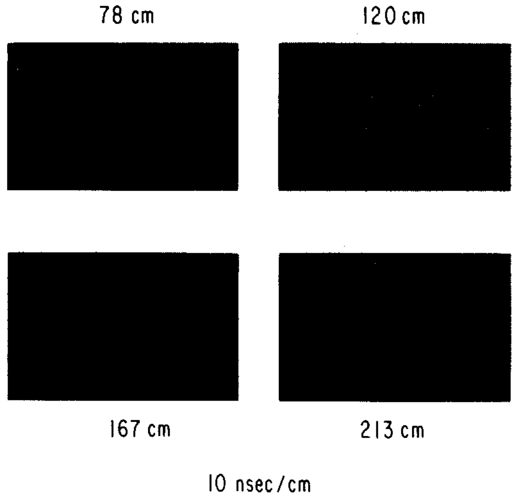

FIG. 19. Real time wave amplitude at four positions in Fig. 17.

the disruption process is not statistical. We have measured the real-time waveform produced by the interference of these waves. This is shown in Fig. 19 at various positions. At $z = 78$ cm, which is near saturation, the modulation is slight because the sidebands are small. As they grow, the modulation becomes quite pronounced as seen at $z = 167$ cm. The particles within these beat minima become untrapped, spread in phase space, and eventually phase mix. This results in a beam "randomization" which precludes further trapping oscillations.

Figure 20 shows the time-averaged velocity distribution measured with and without the sidebands at three positions in Fig. 17. In the single wave case, Fig. 20(a), the distribution is peaked in accordance with the trapping model. At $z = 223$ cm the power in the beam is near its maximum value. As the wave power decreases during the trapping oscillation, the beam regains energy and the peak of the distribution moves back toward the injection velocity. In contrast, Fig. 20(b) shows that when the sidebands destroy the trapping oscillations, the beam distribution is no longer peaked and it changes very little as the instability evolves. These are consistent with the distributions we have obtained in our calculation in which the particles have been mixed in phase space by the additional waves. The linear phase velocities of the larger amplitude waves are indicated. At $z = 256$ cm the average velocity of the flattened distribution is $u_{av} = 0.87\,u_0$ which is slightly slower than the phase velocity of the main wave. The width of the distribution (90% of the particles) is $\Delta u = \pm 0.25\,u_0$ which is roughly equal to the trapping width. Nearly 23% of the particles have velocities greater than the injection velocity.

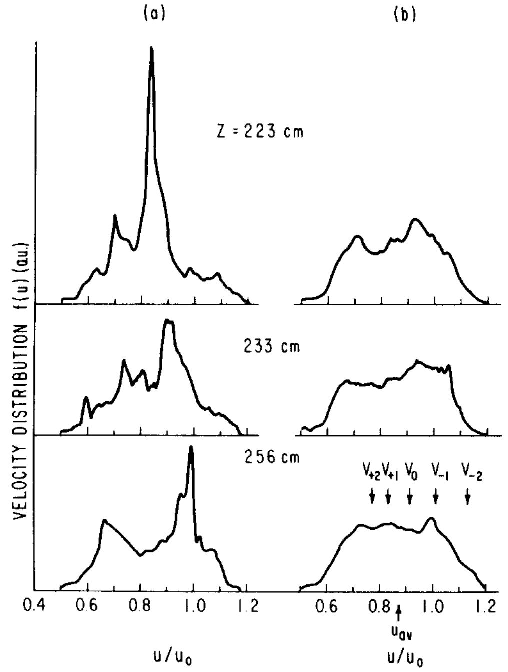

FIG. 20. Phase averaged velocity distribution vs velocity (normalized to injection velocity) at three positions in Fig. 17. (a) Launch ω_0 only. (b) Launch ω_0 and ω_{+1}.

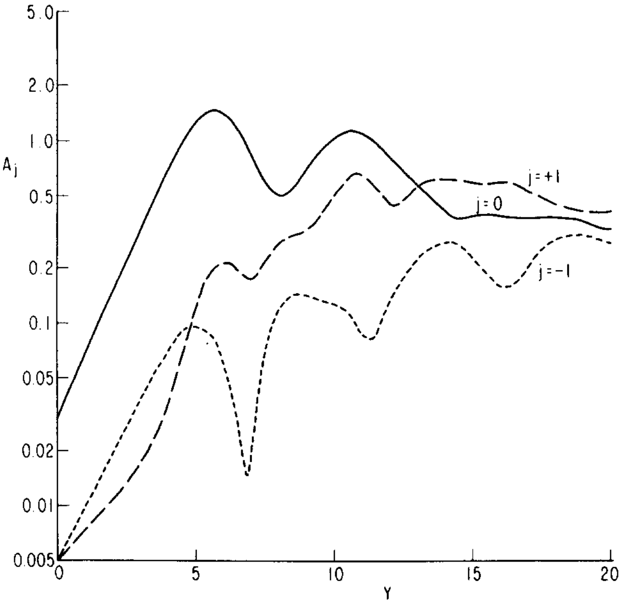

FIG. 21. Computed wave amplitudes vs y for parameters pertinent to experiment in Fig. 17. $A_0(0) = 0.03$, $A_{+1}(0) = A_{-1}(0) = 0.005$, $b_0 = 0.75$, $b_{+1} = 1.75$, $b_{-1} = 0$, and $d_0 = d_{+1} = d_{-1} = 0.03$.

The destruction of the trapping oscillations by sidebands is described well by the numerical solutions to Eqs. (31)–(34). Figure 21 shows the computed amplitudes of the main $(j = 0)$, the slow $(j = +1)$, and the fast $(j = -1)$ waves vs distance for parameters pertinent to the experiment in Fig. 17. Experimentally, we chose the wave frequencies so that $\omega_0/\Delta\omega$ has an integer value; in Fig. 17 $\omega_0/\Delta\omega = 5$. Consequently, we need to follow only the particles whose initial phases are in the interval $0 \leq \phi_0 < 10\pi$ to satisfy the periodic boundary conditions. We keep only the three modes $j = 0, \pm 1$ because experimentally we find that these are the modes which dominate prior to the destruction of the trapping oscillations. They each have the damping coefficient $d = 0.03$. The initial amplitudes are $A_0(0) = 0.03$ and $A_{\pm 1}(0) = 0.005$.

The solutions reproduce the salient features in Fig. 17(b). While the amplitude of the main wave exceeds

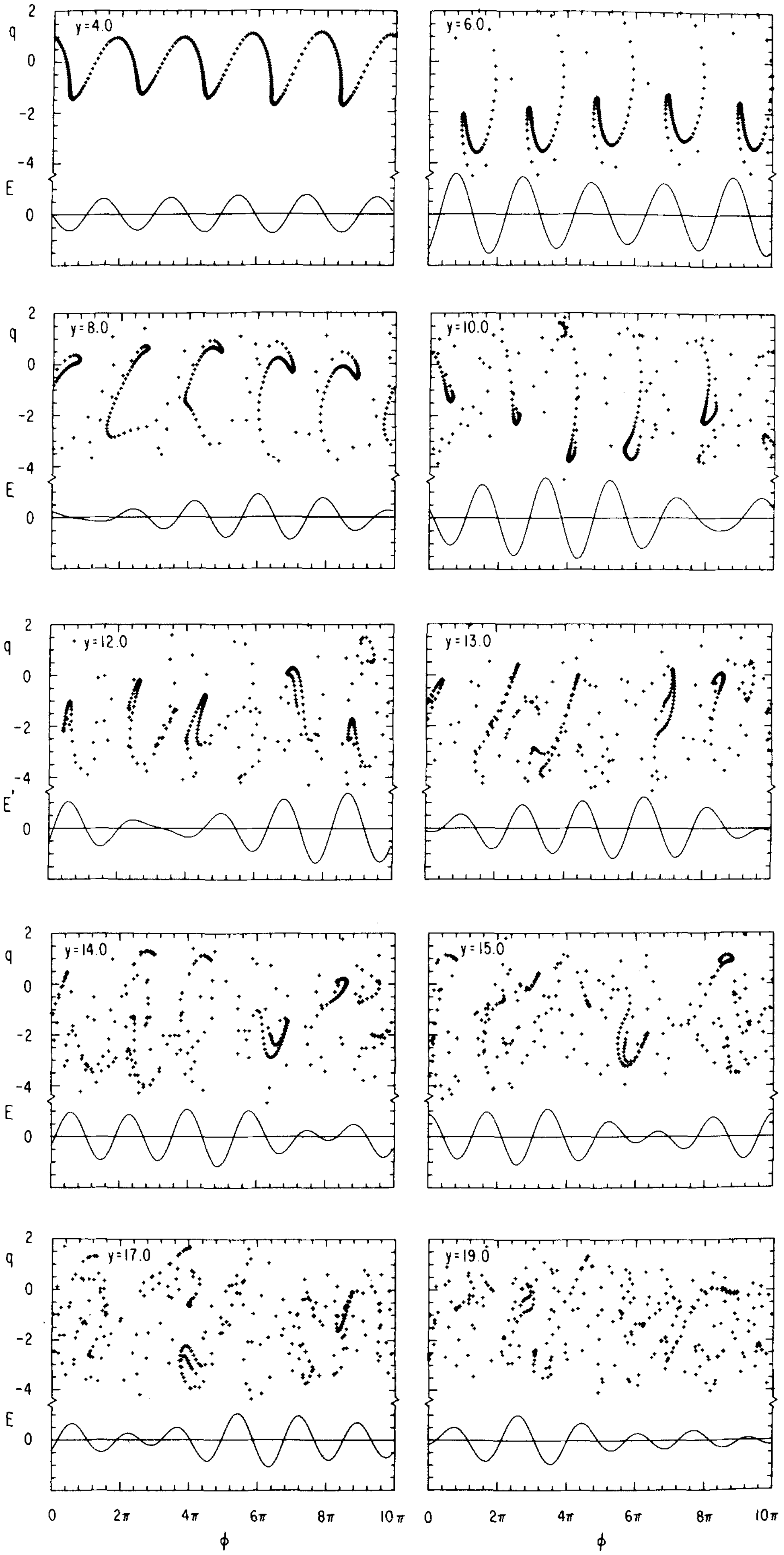

FIG. 22. Phase space dynamics at various positions y for computation in Fig. 21.

those of the satellites, the main wave evolves with the characteristic single wave behavior. However, the satellites continue to grow in the nonlinear region. When they attain amplitudes comparable to the amplitude of the main wave, the trapping oscillations are destroyed. The slow wave overtakes the main wave and then remains 50% larger in amplitude with only mild spatial variation. Its equilibrium amplitude is smaller than the saturation amplitude of the main wave. The predicted amplitudes are 30% larger than observed because the finite C corrections have been neglected.

The particle phase mixing is evident in the phase space plots in Fig. 22. Unlike Fig. 13 the abscissa is the particle phase ϕ in the initial beam frame. In addition to the scaled velocity q, we plot the total electric field, given by Eq. (34), to show the modulation.[37] The force is positive when the field is above the straight line, which indicates $E=0$. When the main wave dominates, the trapped particles oscillate about the zero of E which has a negative slope. As the satellites grow the field becomes modulated. When the interference is destructive, the field is small. The particles within the beat minimum become untrapped momentarily. These previously bunched particles spread and lose their phase relation with the main wave, with many particles actually spilling into adjacent troughs. This results in a local mixing; however, the velocity of the beat minimum, given by the nonlinear group velocity, is generally not equal to the average particle velocity. Consequently, most particles eventually experience the perturbation. The bunches are destroyed and the particles become thoroughly phase mixed as seen at $y=19$.

At $y=17.5$ the average scaled velocity of the particles is $q=-1.3$ with 88% of the particles being within a velocity spread of $\Delta q=\pm 2.25$. According to Eq. (15) with $C=0.12$, these transform to an average velocity $u_{av}=0.84u_0$ and a velocity spread $\Delta u=\pm 0.27u_0$. Both values agree with the corresponding quantities measured at $z=256$ cm.

In typical beam-plasma experiments,[5-10] the main wave is observed to evolve into a broad spectrum during the first trapping oscillation. The beam electrons are spread in velocity and the trapping oscillations are destroyed. We observe similar behavior when we launch broadband noise in addition to the main wave. The noise within the instability bandwidth continues to grow in the nonlinear region until the trapping oscillations are destroyed in a manner similar to that in Fig. 17. However, our result with the single test wave suggests that the statistical nature of the noise is incidental and that the modulation of the main wave, be it statistical or not, is pre-eminent in destroying the trapping.

The disruption process which we have described in this section does not depend on the nature of the linear slow wave structure. Thus, we expect an analogous behavior in a beam-plasma system.

VIII. CONCLUSIONS

We have shown that the trapping oscillations in a traveling wave tube can persist for at least five bounces. In the nonlinear region the wave phase velocity oscillates at $2k_b$ and decreases on average to accommodate the slowed beam particles. Therefore, not only do the trapped particles slosh back and forth in the wave potential, but the phase of the potential oscillates as well. This not only modifies the relation between the bounce length and the wave amplitude, but it also has important consequences with regard to the stability of the trapping.

We have found two ways of destroying the trapping oscillations. The first mechanism involves the main wave only and occurs for finite dissipation in the slow wave sturcture, namely $k_{0i}\simeq 0.08\,C\omega/u_0$. As a result of damping, the wave experiences deep amplitude minima during the trapping oscillations. These trigger large and sudden wave phase shifts which, in effect, transfer many of the particles to phases near the potential maximum in such a manner as to abruptly detrap them. The second mechanism is a result of unstable sidebands growing to amplitudes comparable to the main wave. These sidebands modulate the main wave to produce tiny beat minima which allow the particles to become detrapped. Both detrapping mechanisms lead to particle mixing in phase space which precludes further trapping oscillations. It is noteworthy that these two mechanisms are not statistical in nature.

Following the phase mixing, triggered by either method, the time-averaged velocity distribution is centered near the phase velocity of the main wave and has a velocity spread roughly equal to the trapping width. This state may still be unstable. We have not yet investigated its subsequent relaxation.

All of our experimental results, including the detrapping mechanisms, are corroborated by the numerical solutions of the scaled equations which describe the interaction. Since the interaction in a traveling wave tube is identical to the beam-plasma instability in the small cold beam limit, we expect an analogous behavior in a beam-plasma system.

ACKNOWLEDGMENTS

The authors wish to thank Professor T. M. O'Neil for motivating this experiment and for many useful discussions. It is a pleasure to thank C. C. Cutler for helpful hints concerning the design of the apparatus. The authors are indepted to Dr. T. P. Starke for his contributions. The technical assistance of Mr. G. Smith is greatly appreciated.

This paper is based on a dissertation submitted by G. Dimonte to the University of California at San Diego in partial fulfillment of the requirements for the Ph. D. degree.

This work was supported under National Science Foundation Grant PHY-73-05125-A02.

[1] W. E. Drummond, J. H. Malmberg, T. M. O'Neil, and J. R. Thompson, Phys. Fluids 13, 2422 (1970).

[2] I. N. Onishchenko, A. R. Lineskii, M. G. Matsiborko, V. D. Shapiro, and V. I. Shevchenko, Zh. Eksp. Teor. Fiz. Pisma Red. 12, 407 (1970) [JETP Lett. 12, 281 (1970)].

[3] T. M. O'Neil, J. H. Winfrey, and J. H. Malmberg, Phys. Fluids **14**, 1204 (1971).

[4] T. M. O'Neil and J. H. Winfrey, Phys. Fluids **15**, 1514 (1972).

[5] J. H. Malmberg and C. B. Wharton, Phys. Fluids **12**, 2600 (1969).

[6] J. R. Apel, Phys. Fluids **12**, 640 (1969).

[7] K. Mizuno and S. Tanaka, Phys. Rev. Lett. **29**, 45 (1972).

[8] J. H. van Wakeren and H. J. Hopman, Phys. Rev. Lett. **28**, 295 (1972).

[9] K. W. Gentle and J. Lohr, Phys. Fluids **16**, 1464 (1973).

[10] M. Seidl, W. Carr, D. Boyd, and R. Jones, Phys. Fluids **19**, 78 (1976).

[11] W. L. Kruer, J. M. Dawson, and R. N. Sudan, Phys. Rev. Lett. **23**, 838 (1969).

[12] A. L. Brinca, J. Plasma Phys. **7**, 385 (1972).

[13] N. G. Matsiborko, I. N. Onishchenko, Ya, B. Fainberg, V. D. Shapiro, and Shevchenko, Zh. Eksp. Teor. Fiz. **63**, 874 (1972) [Sov. Phys.-JETP **36**, 460 (1973)].

[14] S. Kainer, J. Dawson, and R. Shanny, Phys. Fluids **15**, 493 (1972).

[15] R. R. Parker and A. L. Throop, Phys. Rev. Lett. **31**, 1549 (1973).

[16] A. Y. Wong and B. H. Quon, Phys. Rev. Lett. **34**, 1499 (1975).

[17] H. Ikezi, R. P. H. Chang, and R. A. Stern, Phys. Rev. Lett. **36**, 1047 (1976).

[18] J. R. Pierce, *Traveling Wave Tubes* (Van Nostrand, New York, 1950).

[19] A. Nordsieck, Proc. IRE **41**, 630 (1953).

[20] R. Kompfner, Inst, Radio Eng. **10**, 283 (1950).

[21] C. C. Cutler, Bell. Sys. Tech. J. **35**, 841 (1956).

[22] J. E. Rowe, IRE Trans. Electron Devices **ED-3**, 39 (1956).

[23] P. K. Tien, Bell. Sys. Tech. J. **35**, 349 (1956).

[24] C. K. Birdsall and G. R. Brewer, IRE Trans. Electron Devices **ED-1**, 1 (1954).

[25] G. M. Branch and T. G. Mihran, IRE Trans. Electron Devices **ED-2**, 3 (1955).

[26] T. M. O'Neil and J. H. Malmberg, Phys. Fluids **11**, 1754 (1968).

[27] R. L. Hess, Aeronautical Systems Division Technical Report 61-15, AD267045 (1961).

[28] M. K. Scherba and J. E. Rowe, IEEE Trans. Electron Devices **ED-18**, 11 (1971).

[29] H. Mishihara, K. Ura, and M. Tereda, IEEE Trans. Electron Devices **ED-18**, 1155 (1971).

[30] P. K. Tien, Proc. IRE **41**, 1617 (1953).

[31] H. R. Johnson, Proc. IRE **43**, 874 (1955).

[32] P. K. Tien, L. R. Walker, and V. M. Wolontis, Proc. IRE **43**, 260 (1955).

[33] G. J. Morales and T. M. O'Neil, Phys. Rev. Lett. **28**, 417 (1972).

[34] P. J. Vidmar, J. H. Malmberg, and T. P. Starke, Phys. Fluids **19**, 32 (1976).

[35] T. M. O'Neil, Phys. Fluids **8**, 2255 (1965).

[36] W. Carr, D. Boyd, H. Liu, G. Schmidt, and M. Seidl, Phys. Rev. Lett. **28**, 662 (1972).

[37] The significance of the modulation of the main wave by the unstable sidebands was recognized by J. H. van Wakeren and H. J. Hopman, J. Plasma Phys. **13**, 349 (1975).